Soft Matter

Multiscale nature of electric-field-induced structural formations in non-colloidal suspensions

Journal:	*Soft Matter*
Manuscript ID	SM-ART-05-2022-000617.R1
Article Type:	Paper
Date Submitted by the Author:	15-Aug-2022
Complete List of Authors:	Mirfendereski, Siamak; University of Nebraska-Lincoln Park, Jae Sung; University of Nebraska -Lincoln, Department of Mechanical and Materials Engineering

Soft Matter

ARTICLE TYPE

Cite this: DOI: 00.0000/xxxxxxxxxx

Multiscale nature of electric-field-induced structural formations in non-colloidal suspensions†

Siamak Mirfendereski and Jae Sung Park*

Received Date
Accepted Date

DOI: 00.0000/xxxxxxxxxx

Non-colloidal suspensions undergoing dipolar interactions in an electric field have been extensively studied and are also known as smart materials as they share similarities with electrorheological (ER) fluids. Although the macroscopic responses are well-documented, the multiscale nature of such suspension is still lacking. In this study, a large-scale Stokesian dynamics simulation is used to investigate the structural formation of such suspensions in an electric field up to highly concentrated regimes across different length scales: from particle-level (microscale) to particle cluster-level (mesoscale) and stress response-level (macroscale). It is observed that at a volume fraction of $\phi \approx 30\%$, the steady-state structures are the most isotropic at the microscale, but at the macroscale, their normal stress fields are the most anisotropic. Interestingly, these structures are also the most heterogeneous at both microscale and mesoscale. Furthermore, the effects of confinement on the multiscale responses are explored, revealing that there could be a strong link between the mesoscale and macroscale. This multiscale nature can offer the potential for precisely controlling or designing ER fluids in practical applications.

1 Introduction

Under an external electric field, the suspended particles with a dielectric constant mismatched with a suspending fluid experience a rapid formation of dipole moment, which leads to particle-particle interactions [1]. This so-called dipolar interaction can cause a relative particle motion toward the formation of anisotropic structures, such as chains and columnar structures, as seeking a lower energy state [1, 2]. As these structures significantly alter the suspension rheology, such electric-field-driven suspensions are often termed electrorheological (ER) fluids [3]. The same driving mechanism of the ER fluid can be generated in a suspension of dielectric particles under a uniform electric field. As the particles disturb a local electric field around them, a non-uniform electric field is created by which particle motion arises along the field gradients. This nonlinear electrokinetic phenomenon is termed dielectrophoresis (DEP) [4, 5].

It has been well-documented that upon the application of an electric field to ER fluids or DEP suspensions at dilute and semi-dilute regimes, particles rapidly form chains along the field direction and then aggregate and form larger structures at long times [6–11]. The particle motion at short times is dominated by the formation of small clusters, while at long times by the interactions between the percolating clusters [10]. The short-term chain formation can be easily explained by the minimum dipole energy that is reached when each of the two dipoles pairs up along the field direction. In contrast, the long-term follow-up rearrangement of structures is still a subject of investigation. Nevertheless, it is suggested that during the long-term structural rearrangement, the slow approaching of the particle chains could be attributed to the net chain-chain attraction [7, 12]. The attractive interaction between the perfectly aligned one-dimensional chains was shown to decay exponentially with chain-chain separation distance, which is called an electrostatic screening effect [7]. However, other longer-range interactions could be possible due to geometrical disorder induced by thermal fluctuation [7] or inevitable intrinsic topological disorder within structures [9], both of which lead to a slower decay rate, the inverse fourth power of the separation distance. In the case of confined suspensions with electrodes, the chains spanning the gap between the electrodes can be repulsive in the range above the certain separation distance [12, 13]. Indeed, the balance between the near-field attraction and far-field repulsion depends on various suspension conditions, such as volume fraction and electrode gap, resulting in different mesostructural features at a steady state [12, 13].

The structures and kinetics of ER fluids or DEP suspensions strongly depend on volume fraction ϕ [10, 14]. Increasing volume fraction results in the progressive loss of the structural anisotropy as body-centered tetragonal (BCT) crystal structures are formed earlier [9]. This BCT structure is known as the ground

Department of Mechanical and Materials Engineering, University of Nebraska-Lincoln, Lincoln, NE 68588-0526, USA. E-mail: jaesung.park@unl.edu

† Electronic Supplementary Information (ESI) available: Movies of periodic and confined suspensions. See DOI: 10.1039/cXsm00000x/

state for ER fluids [6, 7, 15]. The dependence of the structural morphology and transition behavior on volume fraction was also experimentally observed [16]. At $\phi = 10\%$, the ground-state crystal structure is formed from the one-dimensional chains. Beyond $\phi = 15\%$ up to $\phi = 45\%$, the presence of the chains starts to decrease, but the two-dimensional sheets or large particle columns become dominant features, turning to the long-term labyrinthine patterns and eventually BCT crystals. This labyrinthine pattern formation could be related to kinetically arrested gels [17, 18].

From an application perspective, the distinctive rheological characteristics of the ER fluids, such as reversible and controllable viscosity enhancement, have led to a wide range of applications. Examples are active shock absorbers, clutches, brakes, dampers, and actuators [19–22]. In addition, the concept of the ER fluids has been utilized in additive manufacturing of a battery electrode to control micro or nano-structural manipulations of internal structures [23]. The potential of precisely tuning the microstructure by an electric field has also made such fluids appealing in photonic crystal applications [24] and DNA research [25]. The ER fluids are also known to have a potential for a transition to a solid state. Thanks to such intriguing potential, their rheological response to an external flow has been extensively studied [10, 26–29]. The elastic body-like deformation was developed at low shear rates, while the rapid microstructural rearrangement occurred at higher shear rates [27]. In this regard, the Bingham plastic constitutive model was primarily used to describe the rheological behavior of the ER fluids, where their yield stress is shown to scale as the squared electric-field strength, which is indeed the same scale as the dipolar interactions [26, 29].

As presented so far, there have been many studies on the ER fluids and DEP suspensions at up to semi-dilute regimes, focusing on macroscopic measures, namely the stress or viscosity. These measures have been correlated only with structural morphology. Thus, it is evident that understanding the multiscale nature of the structural formation in ER fluids or DEP suspensions is currently lacking. Furthermore, a robust connection among different length scales is largely unexplored because it is highly challenging [30]. However, connecting the macroscopic responses to the particle-level (microscopic) or particle cluster-level (mesoscopic) responses is necessary to promote the fundamental understanding of the underlying mechanisms behind the structural formation of ER fluids and DEP suspensions. Access to mesoscopic scales is also required as it can play a critical role in identifying a hidden linkage between micro and macroscopic responses in a suspension [31, 32].

In this study, we provide for the first time a detailed description of the structural formation across length scales at a wide range of volume fractions up to $\phi = 50\%$ using a large-scale Stokesian dynamics simulation. In addition, the effects of confinement on the multiscale nature of structural formation will also be presented as it has been widely observed that the confinement plays a crucial role in affecting the dynamics and pattern formation in various suspensions [33–36]. Using a detailed algorithm for large-scale simulations presented in Sec. 2, we can probe a long range of time scales in suspensions. Simulation results are presented in Sec. 3, where we start by providing the particle velocity and the mean cluster size as suspension kinetic measures. We then provide measures at three different length scales: (i) the coordination number and fabric tensor as microscopic measures, (ii) the number density fluctuation as a mesoscopic measure, and (iii) the particle-induced stress field as a macroscopic response. The effects of confinement on these scale measures are also provided. We summarize our findings in Sec. 4.

2 Governing equation and simulation method

We consider a suspension of N identical neutrally buoyant spheres of radius a in a viscous electrolyte with the permittivity ε and viscosity η. Two different simulation domains are used, a periodic domain in all three directions for simulating an unbounded infinite suspension and a domain that is periodic in the x and y directions but wall-confined along the z direction (the field direction). The unit cell dimension is denoted by L_x, L_y, L_z, where L_z is the electrode spacing for the confined domain. The particles are assumed to be charged and nonpolarizable, a good approximation for dielectric particles. The Debye layer thickness λ_D of particles is much smaller than the particle size ($\lambda_D \ll a$) by which the particles with their Debye layers behave like insulators so their permittivity does not play a role. We apply an external uniform AC electric field $\boldsymbol{E}_0 = \pm E_0 \hat{\boldsymbol{z}}$ given by the wave of frequency f. The frequency is assumed to be high enough to satisfy both $f \gg D/\lambda_D^2$ and $f \gg \varepsilon\zeta E_0/a\eta$, which validates the assumptions that the Debye layer remains at equilibrium and the particle motion due to linear electrophoresis is negligible, respectively. Note that D is the characteristic diffusivity of the ions in the electrolyte and ζ is the native zeta potential of the particles. In a typical experimental study for an aquatic electrolyte, which is the condition of interest for the current study, $D \sim 10^{-5}$ cm^2 s^{-1}, $\lambda_D \sim 10$ nm and particle radius of $a \sim 10$ μm. Such conditions can be assured for high frequency field $f \sim 1$ MHz [11, 37]. It is also assumed that the particle size is large enough to make Brownian motion negligible. In a typical experiment using a suspension of particles with 10 μm radius and an external field of $E_0 > O(10)$ V/cm, the electric Pećlet number, defined by

$$\mathrm{Pe} = \frac{\varepsilon a^3 E_0^2}{k_B T}, \tag{1}$$

becomes large enough (Pe > 100) to ensure that the effect of Brownian motion is negligible [12]. Note that this dimensionless Pećlet number measures the relative magnitude of particle convection due to dipolar interactions and Brownian diffusion. Under these assumptions, the motion of the particles results entirely from nonlinear dipolar interactions.

For the current simulation, we use the numerical algorithm developed in our previous works [38, 39]. The velocity of each particle $\dot{\boldsymbol{x}}_\alpha$ is computed by a pairwise model [4, 38], and thus can be expressed as

$$\dot{\boldsymbol{x}}_\alpha = \frac{\varepsilon a E_0^2}{\eta} \sum_{\beta=1}^{N} \mathbf{M}(\boldsymbol{R}_{\alpha\beta}/a) : \hat{\boldsymbol{z}}\hat{\boldsymbol{z}}, \qquad \alpha = 1, \ldots, N \tag{2}$$

where $\boldsymbol{R}_{\alpha\beta} = \boldsymbol{x}_\beta - \boldsymbol{x}_\alpha$ is the separation vector between particle α and particle β, and $\mathbf{M}$ is a third-order dimensionless tensor, which

is a function of the relative configuration of a pair of spheres. It is shown that tensor $\mathbf{M}$ is entirely determined by three scalar functions of the dimensionless inverse separation distance, $\lambda = 2a/|\boldsymbol{R}|$ [4]. For widely separated spheres (typically when $|\boldsymbol{R}_{\alpha\beta}| > 4a$), the far-field expression of tensor $\mathbf{M}$ is derived as follows using the method of reflection:

$$\mathbf{M}_{FF}(\boldsymbol{R}/a) = \frac{1}{12}\mathbf{T}(\boldsymbol{R}/a) + O(\lambda^5), \tag{3}$$

where $\mathbf{T}$ is the Green's functions for a potential quadrupole [40] and given in index notation as follows:

$$T_{ijk}(\boldsymbol{R}) = -\frac{6}{R^5}(\delta_{ij}R_k + \delta_{ik}R_j + \delta_{jk}R_i) + 30\frac{R_iR_jR_k}{R^7}. \tag{4}$$

We use a periodic version of Eq. 3 to account for the interaction of particle α with particle β in the computational domain, along with the periodic images of particle β in all three directions. This far-field tensor is asymptotically valid to order $O(\lambda^4)$ for any pair of particles. However, if particle α and β are close to each other (typically when $|\boldsymbol{R}_{\alpha\beta}| < 4a$), the far-field tensor in Eq. 3 becomes inaccurate. To that end, $\mathbf{M}_{FF}$ is replaced by the more accurate version tensor $\mathbf{M}_{TM}$ calculated by using the method of twin multiple expansions for a near-field interaction [4]. This method is accurate down to a separation distance of $|\boldsymbol{R}_{\alpha\beta}| \approx 2.005a$. Note that the particle velocity from Eq. 2 with $\mathbf{M}_{FF}$ and $\mathbf{M}_{TM}$ accounts for both electric and hydrodynamic interactions between the particles. For the confined domain, only periodic images of particles in the x and y directions are considered. For particle-wall interactions, only short-range interactions with the boundaries are captured to focus on an effect on particle dynamics in the vicinity of the electrodes[12], while long-range interactions could be possible [41] but will be included in future work.

Direct calculation of Eq. 2 requires the high-order computation $O(N^2)$, which makes the simulation of many particles prohibitively expensive. Hence, the fast smooth particle mesh Ewald (SPME) algorithm based on the Ewald summation formula of Hasimoto [42] and on fast Fourier transforms is employed to accelerate the computation to $O(N\log N)$ [43]. The SPME algorithm is another version of the accelerated Stokesian dynamics simulation [44]. This algorithm has been extended to Stokes dipole and potential quadrupole interactions [12, 38]. Here, a fixed time step Δt is used and chosen to ensure that particles only travel a fraction of the mean inter-particle distance during one integration step. To prevent excessive particle overlaps, which occur due to the use of finite time steps in simulations, we implement an effective algorithm, functionally identical to the potential-free algorithm [17], where the particles are moved almost exactly within roundoff errors ($\sim 2.005a$), to contact. This potential-free algorithm has been added to the simulation model in our previous works [39, 45] for simulating very concentrated suspensions. In the remainder of the paper, all variables are made dimensionless using the characteristic length scale $l_c = a$ and time scale $t_c = \eta/\varepsilon E_0^2$.

3 Results and discussion

We consider a suspension in a domain of dimension $L_x \times L_y \times L_z = 40^2 \times 20$ for a range of volume fractions ϕ up to $\phi = 50\%$. All simulations are initiated from the hard-sphere equilibrium configurations at a given volume fraction. To check the dependence of the initial configuration, we have run multiple simulations with different initial configurations for each volume fraction, confirming that the overall structural dynamics are insensitive to the initial configuration.

3.1 Bulk suspension

The time evolution of the particle distribution in a suspension for volume fractions of $\phi = 15\%$ and 30% is shown in Fig. 1. At $t = 0$, particles are randomly distributed, and an electric field is applied, which, in response, leads to the formation of particulate structures over time. Shown in Fig. 1(a) for $\phi = 15\%$, the particles initially chain up along the field (z) direction on a fast time scale of $O(200)$. This fast process is then followed by the rearrangement of the chains on a longer time scale. The structural rearrangement coincides with the coalescence of the nearby chains, resulting in the formation of larger structures like thick columnar aggregates [12]. Fig. 1(b) shows a suspension at $\phi = 30\%$. There is a noticeable difference in the structural evolution compared with $\phi = 15\%$. The particles do not seem to form initial chain-like structures. Instead, they tend to directly undergo the formation of mesoscopic structures larger than thick columnar aggregates. This early formation of the mesoscopic cellular pattern is observed by the formation of particle-free voids in a suspension at up to $t \approx 400$. As these voids tend to expand with time due to the continuous rearrangement and coalescence of structures, sizable clusters are eventually formed. A suspension then becomes nearly steady-state at $t > 1400$. Note that the particle motion within structures seems to slow down at $t \approx 400$ for both volume fractions, and the structures do not evolve significantly after $t = 1400$.

The kinetics of the suspension evolution is then quantified by the ensemble-averaged root-mean-square (RMS) particle velocity u_{rms}. Fig. 2 shows the RMS velocity at different volume fractions as a function of time. As soon as the electric field is applied, the particle motion instantaneously arises as a result of dipolar interactions between particles. Since particle pairing due to the dipolar or dielectrophoretic effects is inherently stable, the particle velocity continues to decrease over time until the particle motion almost ceases at long times. However, there is a distinct difference in the decreasing trend of u_{rms} for different regimes of volume fractions. For dilute regimes, such as $\phi < 20\%$, there are two characteristic slopes as seen for $\phi = 10\%$ in Fig. 2 – an initial gentle slope followed by a steeper slope after $t \approx 100$. The initial gentle slope represents a slow decay of the velocity, indicating the rapid formation of particle chains along the field direction. The following steeper slope represents a rapid decay of the velocity, corresponding to the rearrangement and coalescence process of the chains, which results in the formation of thicker columnar structures, as seen in Fig. 1(a). However, beyond semi-dilute regimes, roughly for $\phi > 25\%$, there is no initial gentle slope, and

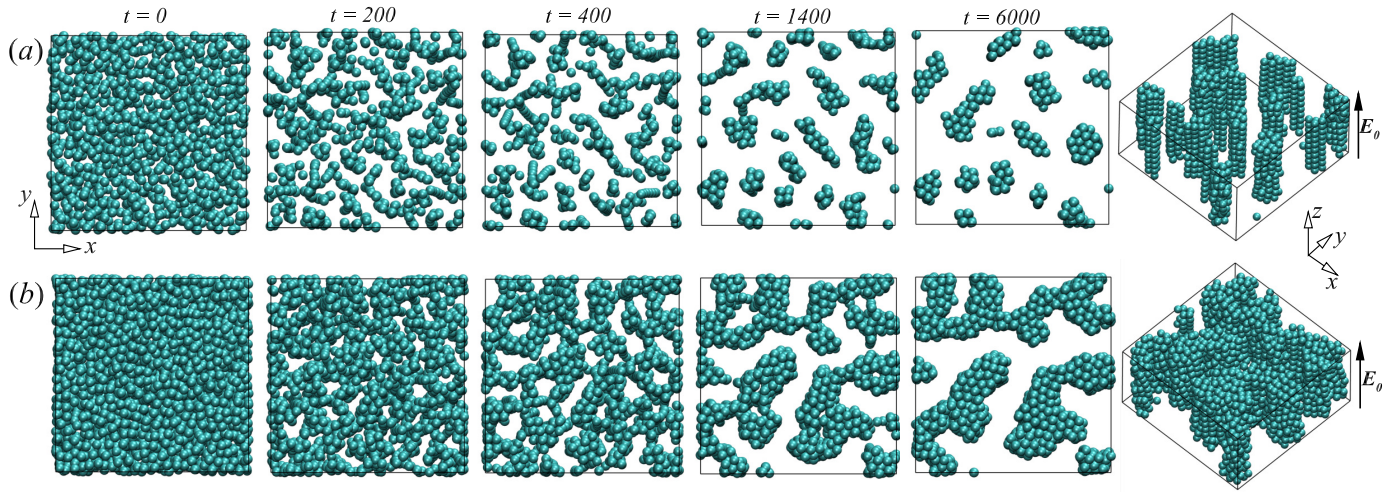

Fig. 1 The temporal evolution of the particle distributions in the $x-y$ plane in a periodic cell of dimensions $L_x \times L_y \times L_z = 40^2 \times 20$. The panel (a) is for $\phi = 15\%$, and the panel (b) for $\phi = 30\%$. The figures at the far right in each panel illustrate the three-dimensional particle distributions at $t = 6000$ or steady state.

the RMS velocity starts to rapidly decrease from the beginning. It again suggests that for the semi-dilute and concentrated regimes, the particles tend to undergo the formation of larger structures directly without forming any initial particle chains, which is consistent with the observations in snapshots in Fig. 1(b). It is worth noting that the suspension reaches an almost steady state when $u_{rms} \approx 0.0017$ as the structures barely evolve and move, although there are very small particle motions within the structures. Hereinafter, we denote the steady-state when $u_{rms} < 0.0017$ in a suspension.

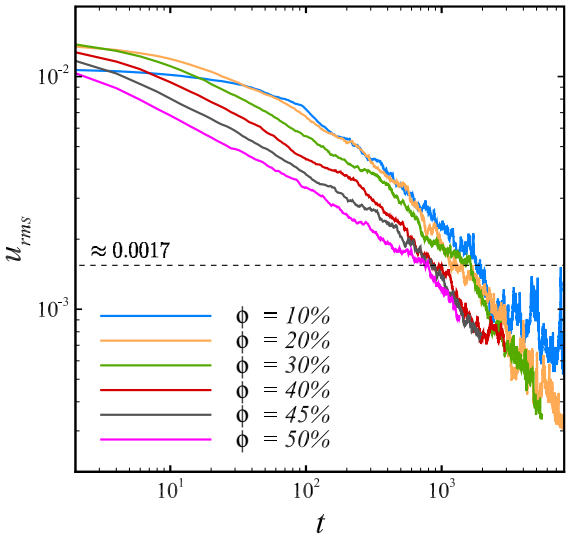

Fig. 2 (Colour online) Temporal evolution of the root-mean-squared (RMS) velocity of particles for various volume fractions. It is found that the suspensions become steady state when $u_{\rm rms} \approx 0.0017$.

To quantify the formation kinetics of the suspension structures, we calculate the mean cluster size S_m as a function of time, which was given by See and Doi [46] as follows

$$S_m(t) = \frac{1}{N} \sum_{k=1}^{N_c(t)} N_k^2(t), \tag{5}$$

where $N_c(t)$ is the number of clusters at a certain time t and N_k is the number of particles in the kth cluster. The cluster statistics are computed by the connectivity matrix method based on the algorithm developed by Sevick *et al.* [47]. In this method, individual clusters are identified by directly-connected and indirectly-connected particles within a cluster. Particle pairs are considered as directly-connected when the separation distance is within a criterion of $|\boldsymbol{R}|/a < 2.0075$. A search for the directly-connected and indirectly-connected particles continues until the individual clusters are identified, given the fact that every particle within a cluster should be connected, either directly or indirectly. The number and size of clusters are then calculated.

Fig. 3 shows a temporal evolution of the mean cluster size computed by Eq. 5 for various volume fractions. For a reference, the dashed line for $S_m = 2$ was added to represent a particle pair from which the time scale of the particle pairing can be estimated at each volume fraction. The characteristic time scale of particle pairing decreases with volume fraction due to the smaller average separation distances between particles in initial random configurations as a volume fraction is increased. At $\phi \leqslant 20\%$, the mean cluster size appears to increase following a power-law function after $S_m > 2$ before reaching a plateau. The exponent of the power-law function slightly increases with volume fraction in this range of volume fractions. Interestingly, the steady-state value of S_m increases a bit larger from $\phi = 10\%$ to $\phi = 15\%$ and also from $\phi = 20\%$ to $\phi = 25\%$ than from $\phi = 15\%$ to $\phi = 20\%$. These observations imply the probabilities of transitions in structural formation among these volume fractions. At $\phi > 30\%$, each

curve starts with an initial small power-law exponent followed by a much higher power-law exponent before reaching a clear plateau of the mean cluster size. As a volume fraction is further increased, these power-law exponents get larger, and the mean cluster size reaches a plateau much faster.

Now, we proceed to presenting the multiscale characteristics of the structural formation at three different scales, namely microscale, mesoscale, and macroscale.

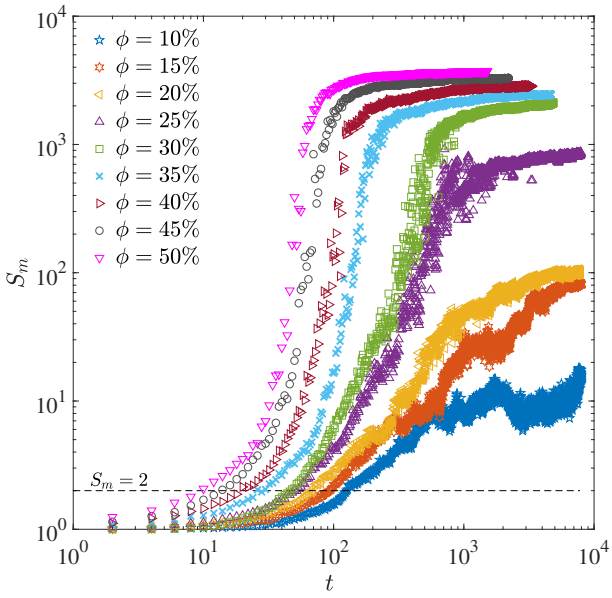

Fig. 3 (Colour online) Temporal evolution of the mean cluster size S_m for various volume fractions. The dashed line indicates the time scales of particle pairing in the field direction at each volume fraction.

3.2 Microscopic measure

To provide a microscopic (particle-level) measure or microstructural information, we first measure the coordination number Z, which represents the average number of neighbor particles in contact with a certain particle. Fig. 4(a) shows the temporal evolution of the ensemble-averaged coordination number $\langle Z \rangle$ at various volume fractions. The two different growth behaviors are observed, where there is an initial fast growth followed by much slower growth at longer times. The inset of Fig. 4(a) shows the steady-state coordination number as a function of volume fraction. As expected, it increases monotonically with volume fraction and especially becomes an almost linear function of volume fraction for $\phi > 15\%$.

More notably, suspensions exhibit interesting behaviors with regard to the microscopic fluctuations. To this end, the standard deviation σ_Z of the ensemble-averaged coordination number Z is calculated. Fig. 4(b) shows the temporal evolution of the normalized fluctuation magnitude $\sigma_Z^2/\langle Z \rangle$ at various volume fractions. This normalized fluctuation magnitude could also be indicative of microscopic heterogeneity. To be more specific, the microscopic heterogeneity can be referred to as the variability in

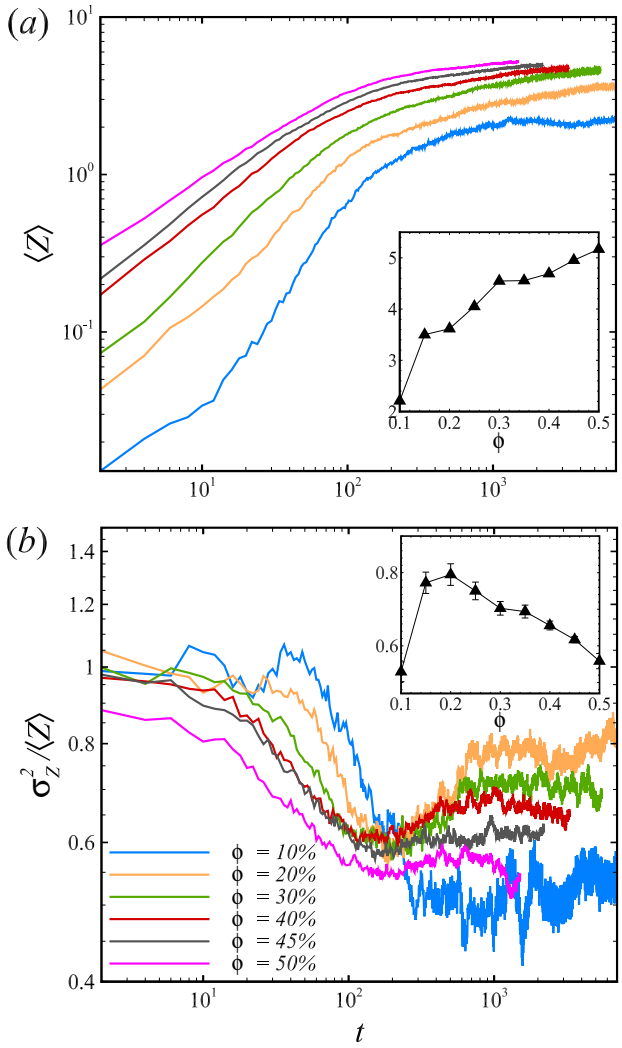

Fig. 4 (Colour online) Temporal evolution of (a) the ensemble-averaged coordination number $\langle Z \rangle$ and (b) the normalized coordination number fluctuation for various volume fractions on log-log scale. Note that σ_z denotes the standard deviation of the ensemble-averaged coordination number. The insets show the time-averaged values of these variables over a steady state as a function of volume fraction.

the coordination number. Initially, the fluctuation decreases as the particles start to form particle chains or bonds, which means that the degree of the microscopic heterogeneity decreases. It then reaches the minimum at about the same time when the average coordination number $\langle Z \rangle$ becomes almost plateau, as seen in Fig. 4(a). Typically, the time at which the fluctuation reaches the minimum decreases with volume fraction. Once the minimum reaches, the microscopic fluctuation exhibits an interesting behavior for different volume fractions. At $\phi = 10\%$, the fluctuation shows a relatively strong variation but stays near its minimum value. For $10\% < \phi < 40\%$, the fluctuation starts to increase until reaching the steady plateau with less variations compared to one for $\phi = 10\%$. This fluctuation growth appears to result from the rearrangement and coalescence of structures during the coarsening process after the particle pairing process. At much

higher volume fractions ($\phi > 40\%$), this growth trend depreciates due to the strong particle loading effects. The inset of Fig. 4(b) shows the time-averaged coordination number fluctuations over a steady-state. Interestingly, the steady-state coordination number fluctuation (i.e., microscopic heterogeneity) exhibits a non-monotonic variation with volume fraction. The microscopic heterogeneity is enhanced with volume fraction and reaches a maximum at $\phi = 20\%$ followed by a subsequent decrease. It suggests that there is a microstructural transition arising at $\phi \approx 20\%$ at which the suspension reaches the most heterogeneous state at the microscale.

To further characterize the microstructure of a suspension, we employ the fabric tensor concept, which was originally introduced for the contact network of granular materials [48, 49]. The fabric tensor $\mathbf{A}^p$ can be computed at the particle level using the following expression [31, 50, 51],

$$\mathbf{A}^p = \sum_{i=1}^{N_b} \boldsymbol{n}_i \otimes \boldsymbol{n}_i, \tag{6}$$

where N_b is the number of the particles in contact, $\boldsymbol{n}_i$ is the unit vector connecting the center of a particle to the center of its ith bond neighbors, and $\otimes$ denotes the dyadic product. The system-sized fabric tensor $\mathbf{A}$ can be then derived by averaging the particle-level fabric tensors over the particle ensemble,

$$\mathbf{A} = \frac{1}{N} \sum_{p=1}^{N} \mathbf{A}^p. \tag{7}$$

The isotropic scalar of the fabric tensor, defined by the trace of $\mathbf{A}$ or tr$\mathbf{A}$, indeed represents the average coordination number. Subtracting this isotropic part from the fabric tensor (i.e., $\zeta = \mathbf{A} - (\text{tr}\mathbf{A}/3)\mathbf{I}$) yields the deviatoric tensor ζ [31], which is illustrative to quantify the microstructural anisotropy. When the diagonal entities of the deviatoric tensor get smaller and close to zero, particle bonds inside the structure exhibit less preference of orientation in all directions, suggesting an isotropic state. Fig. 5(a) shows the temporal evolution of the diagonal entities of the deviatoric tenor ζ in three (x, y, z) directions at various volume fractions. Shortly after applying the electric field to the most isotropic state at $t = 0$, a suspension starts to deviate from its isotropic state at $t \approx 10$, where ζ_{zz} increases and becomes positive, while ζ_{xx} and ζ_{yy} decrease and become negative. The positive sign suggests that the orientation of particle arrangements is preferred in the field direction for $t > 10$. At a specific time (which varies with volume fraction within the range of $t = 110 - 300$), ζ_{xx} and ζ_{yy} become minimum, while ζ_{zz} becomes maximum. The suspensions at that specific time are the most microscopically anisotropic at each volume fraction.

Interestingly, after reaching the most anisotropic state, the long-term behavior of ζ_{xx}, ζ_{yy} and ζ_{zz} appears to depend on volume fraction. At a volume fraction of 10%, the long-term variation of the deviatoric components is almost negligible, meaning that the most anisotropic state continues to maintain. That can be explained by the weak interactions between the highly-anisotropic chain-like structures that are largely separated and hence do not tend to coalesce and rearrange. This explanation is also consistent with the cluster size in Fig. 3, where the mean cluster size for $\phi = 10\%$ remains around 10 at steady state, which is the size of L_z, as most structures are one-dimensional chains spanned in the field direction due to very weak chain-chain interactions. For $15\% \leqslant \phi \leqslant 30\%$, however, the magnitude of ζ_{xx}, ζ_{yy} and ζ_{zz} exhibits a noticeable decrease before reaching a plateau. This decreasing period indicates that the rearrangement and coalescence of the structures arise during this period, leading to the microstructure being more isotropic. For $\phi \geqslant 40\%$, the microscopic anisotropy does not change over time once the most anisotropic state reaches. In this highly concentrated regime, once the suspension reaches its most anisotropic state by forming a cellular network with larger cells of particle clusters, structural evolution tends to arrest without any further microstructural changes.

Fig. 5(b) shows the time-averaged deviatoric components over a steady-state. In this figure, we observe a non-monotonic behavior with volume fraction, which is also seen in the coordination number fluctuation (microscopic heterogeneity) as shown in the inset of Fig. 4(b). However, the deviatoric components show the opposite characteristics to the microscopic heterogeneity. While microscopic heterogeneity increases with volume fraction up to $\phi = 20\%$, the degree of microscopic anisotropy decreases with volume fraction and becomes minimum at $\phi = 30\%$ followed by a subsequent increase. It suggests that there is a microstructural transition arising at $\phi = 30\%$ at which the suspension reaches the most isotropic state at the microscopic level. The most isotropic state results from the fact that the structure becomes much thicker in the x and y directions at $\phi = 30\%$. This makes the particles bond with almost the same number of neighbor particles in all directions. Increasing the volume fraction beyond $\phi = 30\%$ then results in microstructure to be more anisotropic, while becoming more homogeneous.

3.3 Mesoscopic measure

Moving towards the next scale measure at the mesoscale (particle clusters-level), we consider the number density fluctuation as it could provide a measure for the mesoscopic structural information of suspensions, especially mesoscopic heterogeneity [32]. The number density fluctuation can be readily calculated at arbitrary cluster sizes [32, 38, 39]. In this calculation, a probe cell of a fixed volume V is positioned arbitrarily in a simulation domain, where the fixed volume V is chosen a priori. In practice, the number of particles N_p inside the probe cell may differ from the expected value $\langle N_p \rangle = \phi V / V_p$, where $V_p = 4\pi a^3/3$ is the volume of a particle. Note that $\langle N_p \rangle$ represents the expected number of particles inside the cell or the mean cluster size. Quantifying a local variation in the number density of particles, the variance of N_p (i.e., $\sigma^2_{N_p}$) normalized by the expected value $\langle N_p \rangle$ can give the number density fluctuation.

Fig. 6 shows the time-averaged number density fluctuation over steady state as a function of volume fraction for five different expected cluster sizes $\langle N_p \rangle$. For all these five cases, the mesoscopic fluctuations display a non-monotonic behavior as a function of volume fraction. As increased with volume fraction at

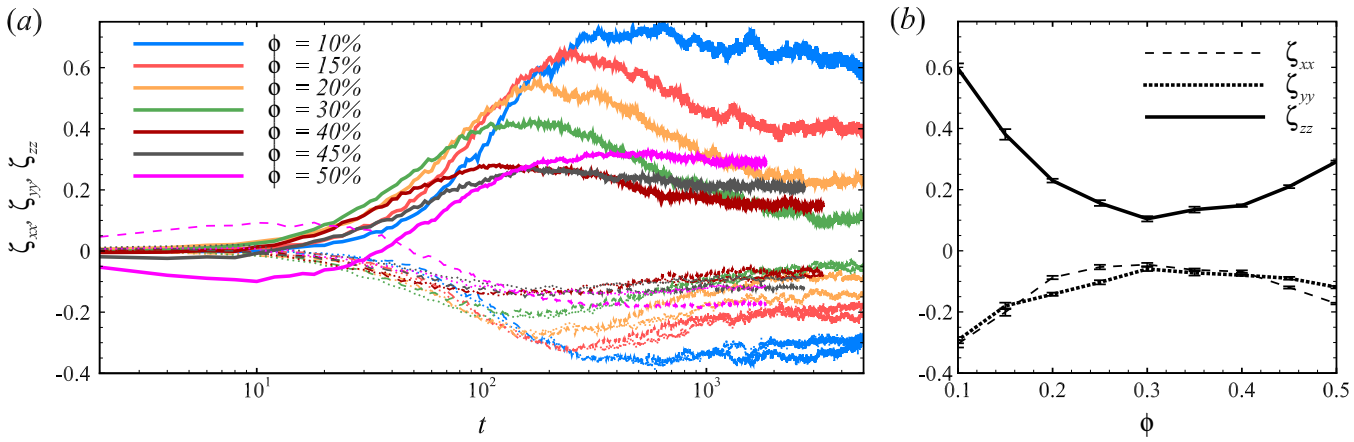

Fig. 5 (Colour online) (a) The diagonal components of the deviatoric tensor, ζ_{xx}, ζ_{yy}, ζ_{zz}, as a function of time for various volume fractions. Due to symmetry with respect to the field direction, $\zeta_{xx} \approx \zeta_{yy}$. Note that the dashed line, dotted line, and solid line represent x, y, and z directions, respectively. (b) The time-averaged diagonal components of the deviatoric tensor over a steady state as a function of volume fraction. A non-monotonic behavior is observed for all three components as a function of volume fraction.

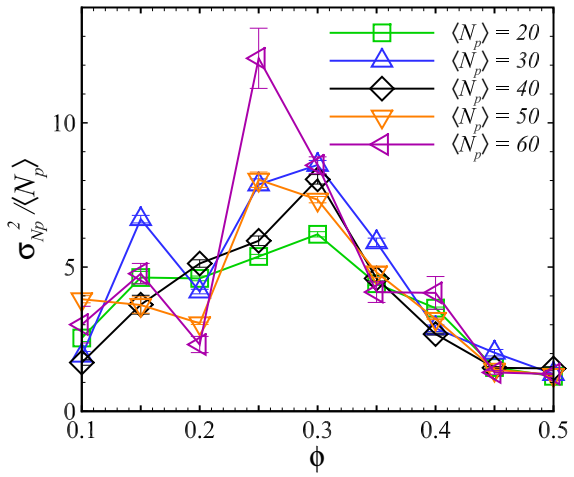

Fig. 6 (Colour online) The number density fluctuation averaged over a steady state as a function of volume fraction. Five different expected values of $\langle N_p \rangle$ are considered, and all cases show the same non-monotonic trend with volume fraction.

$\phi = 10\%$, the maximum values are reached at $\phi \approx 30\%$, suggesting that the suspension becomes the most heterogeneous state at the mesoscale at this volume fraction. As seen in the steady-state particle distribution in Fig. 1, the suspension exhibits a unique particle distribution at steady state at this volume fraction, where there are well-separated large clusters or aggregates that are densely packed with particles. For $\phi > 30\%$, the mesoscopic fluctuation decreases with volume fraction as the particles assemble into a cellular network pattern with smaller particle-free voids. It should be noted that the highly heterogeneous mesoscopic state could tie closely to the highly heterogeneous microscopic state due to large variability in the coordination number.

3.4 Macroscopic measure

To provide a measure for the macroscopic response during the structural evolution, we calculate the particle stress tensor $\boldsymbol{\Sigma}^p$ in a suspension. To leading order, the particle stress mainly results from the dielectrophoretic force $\boldsymbol{F}^{\mathrm{DEP}}$, which to leading order is $O(R^{-4})$. The resulting stress $\boldsymbol{xF}^{\mathrm{DEP}}$ then becomes the leading order of $O(R^{-3})$. Note that the hydrodynamic contribution to the stress is of $O(R^{-5})$, which corresponds to the leading order of the gradient of Eq. 4. The particle stress due to the dielectrophoretic force $\boldsymbol{F}^{\mathrm{DEP}}$ is calculated by

$$\boldsymbol{\Sigma}^p = -n\langle \boldsymbol{xF}^{\mathrm{DEP}} \rangle, \tag{8}$$

where n is the number density of particles and $\boldsymbol{x}$ is the position vector of a particle. The dielectrophoretic force between a pair of particles can be expressed as $\boldsymbol{F}^{\mathrm{DEP}} = 4\pi\varepsilon a^2 \mathsf{F} : \boldsymbol{E}_0\boldsymbol{E}_0$ [4, 38], where the dimensionless third-order tensor F can be written in indicial notation by

$$F_{ijk} = f(\lambda)(\delta_{ij}\hat{R}_k + \delta_{ik}\hat{R}_j) + g(\lambda)\hat{R}_i\delta_{jk} + h(\lambda)\hat{R}_i\hat{R}_j\hat{R}_k, \tag{9}$$

where $\hat{\boldsymbol{R}} = \boldsymbol{R}/|\boldsymbol{R}|$ and $\lambda = 2a/|\boldsymbol{R}|$. The scalar functions f, g, and h can be calculated using the methods of reflection for the asymptotic results and corrected using the twin multipole expansion when the particles are very close to each other [4, 38]. To leading order for the particle stress, the scalar functions are given by

$$f(\lambda) = -\frac{3}{64}\lambda^4,\ g(\lambda) = -\frac{3}{64}\lambda^4,\ h(\lambda) = \frac{15}{64}\lambda^4. \tag{10}$$

Figs. 7(a) and (b) show the temporal evolution of the normal components of the particle stress tensor $\boldsymbol{\Sigma}^p$ in the transverse (x) direction and the field (z) direction, respectively. For all volume fractions, the transverse normal stress Σ^p_{xx} remains negative and becomes more negative after early plateau periods. The time at which the magnitude of Σ^p_{xx} starts to decrease gets earlier with increasing volume fraction as a result of the reconfiguration and coalescence of initially formed structures. For the field normal

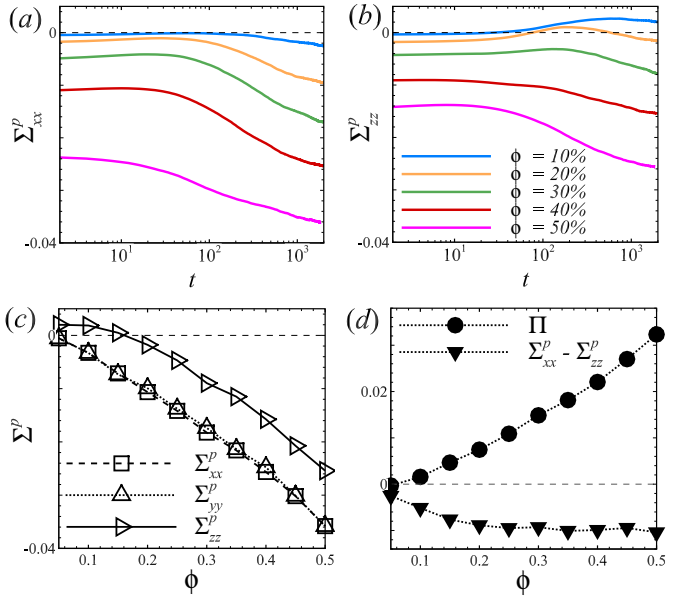

Fig. 7 (Colour online) Time evolution of the diagonal components of the particle stress tensor $\mathbf{\Sigma}^p$. (a) Σ^p_{xx} and (b) Σ^p_{zz} as a function of volume fraction. Note that $\Sigma^p_{yy} \approx \Sigma^p_{xx}$. (c) The time-averaged Σ^p_{xx}, Σ^p_{yy}, and Σ^p_{zz} over steady state as a function of volume fraction. (d) The particle pressure Π and the normal stress difference $\Sigma^p_{xx} - \Sigma^p_{zz}$ over a steady state as a function of volume fraction.

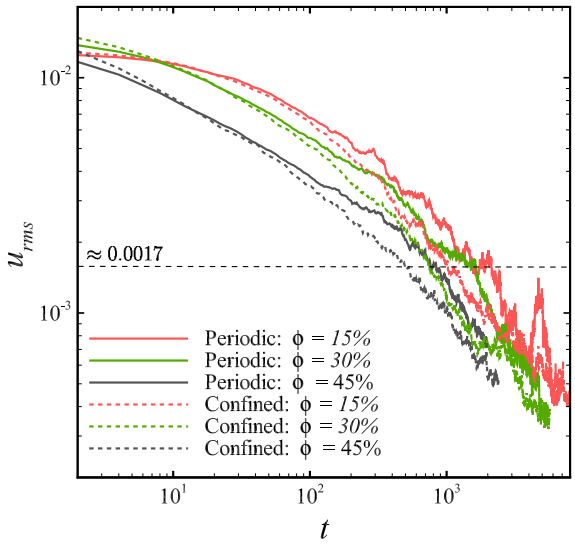

Fig. 8 (Colour online) Temporal evolution of the root-mean-squared (RMS) velocity of particles at three different volume fractions for periodic and confined suspensions.

stress Σ^p_{zz}, the different temporal behaviors are observed between $\phi < 30\%$ and $\phi > 30\%$. For semi-dilute and concentrated suspensions at $\phi > 30\%$, Σ^p_{zz} exhibits almost the same trend as Σ^p_{xx}, while at $\phi = 30\%$, there is a slight go-up before becoming more negative. However, for $\phi < 30\%$, Σ^p_{zz} exhibits a notable non-monotonic variation with time. It goes up after the early short plateau periods. Especially, at $\phi = 10\%$ and 20%, Σ^p_{zz} becomes positive, while it becomes negative again at long times for $\phi = 20\%$.

Fig. 7(c) shows the time-averaged Σ^p_{xx} and Σ^p_{zz} over a steady state as a function of volume fraction. Both normal stresses exhibit a monotonic decreasing trend with volume fraction. As expected, $\Sigma^p_{xx} \approx \Sigma^p_{yy}$ due to symmetry with respect to the field direction. As in the case of hard-sphere suspensions [52], all normal stresses are negative, but interestingly except for positive Σ^p_{zz} at $\phi \leqslant 15\%$. This positive normal stress might result from relatively strong compression in the field direction. For the magnitude of the normal stresses, the transverse stresses Σ^p_{xx} and Σ^p_{yy} are larger than the field stress Σ^p_{zz} due to limited particle motions in the field direction at steady state. To further examine the macroscopic measure at steady state, Fig. 7(d) shows the particle pressure $\Pi = -1/3\Sigma^p_{ii}$ and the normal stress difference $\Sigma^p_{xx} - \Sigma^p_{zz}$. Similar to the hard-sphere suspensions in a shear flow [52, 53], the particle pressure Π is positive and monotonically increases with volume fraction. The normal stress difference becomes more negative with volume fraction and then remains almost constant for $\phi \geqslant 25\%$. In other words, the normal stresses become more anisotropic with volume fraction until its most anisotropic state is reached at $\phi \approx 25\%$. As the volume fraction is further increased, however, the degree of macroscopic anisotropy remains the same even though the particle pressure keeps increasing. Interestingly, the highly anisotropic macroscopic state arises when the structure becomes less anisotropic at the microscale.

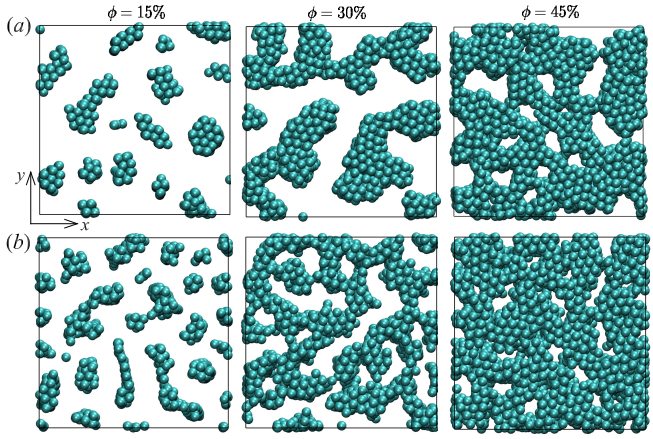

Fig. 9 The steady-state particle distributions at three different volume fractions: the panel (a) for periodic suspensions and the panel (b) for confined suspensions. Movies of periodic and confined suspensions at each volume fraction are included in the ESI.†

3.5 Effect of confinement

Lastly, we evaluate the effects of confinement on the multiscale responses embedded in the suspension. Flat boundaries are present at $z = 0$ and $z = L_z = 20a$, where the periodic interactions are prohibited in the field direction. The simulation method is similar to our previous works [12, 45]. Fig. 8 shows the temporal evolution of the suspension kinetics u_{rms} for both periodic and confined domains. The RMS particle velocity in the confined suspensions tends to decrease faster than for the periodic ones. Similar to

the kinetics in the periodic suspensions, the steady-state seems to arise for the confined suspensions when $u_{rms} \approx 0.0017$ as the structures barely evolve. Figs. 9(a) and (b) show the particle distributions at steady state in the $x-y$ plane for the periodic and confined suspensions, respectively. At $\phi = 15\%$, the confinement makes the suspension form more sheet-like thin aggregates, which are also observed in the previous studies [12, 16]. Similarly, at $\phi = 30\%$, the steady-state pattern of the confined suspension is far different from that of the periodic one. Sizable clusters that are densely packed with particles are well-separated for the periodic case, while a more labyrinthine-like pattern is formed for the confined case. At $\phi = 45\%$, the confinement is likely to make the particle-free voids in a cellular network pattern much smaller than for the periodic case. Movies of periodic and confined suspensions at each volume fraction are included in the ESI.†

The effects of confinement on the multiscale responses in the suspension are investigated across length scales. For the microscale, we again consider the coordination number fluctuation and the deviatoric tensor at a steady state. As seen in Figs. 10(a) and (b), no significant changes are observed in the microscopic responses at least for the current degree of confinement, although the coordination number fluctuation is slightly reduced by confinement. However, for the mesoscale, there is a noticeable change due to confinement. Fig. 10(c) shows the number density fluctuations at steady state for the periodic and confined suspensions. The confinement seems to primarily alter the mesoscopic response, specifically affecting the mesoscopic heterogeneity. Unlike the periodic suspension, where there is a non-monotonic behavior of the fluctuation with volume fraction, the confined suspension shows an almost monotonic decay of the fluctuation with volume fraction. Indeed, the confinement tends to diminish the mesoscopic heterogeneity and eventually removes the most mesoscopically heterogeneous state at $\phi \approx 30\%$. For the macroscale, no significant changes are again made by confinement, as can be seen in the particle pressure and the normal stress difference in Fig. 10(d). It should be noted, however, that the normal stress difference seems to continue to decrease even after $\phi = 25\%$ for the confined suspension, while that of the periodic suspension stays almost constant after $\phi = 25\%$. These confinement effects could suggest that the macroscopic response seems to link more to the mesoscopic features than the microscopic ones, for which detailed investigations will be a subject of interesting future work.

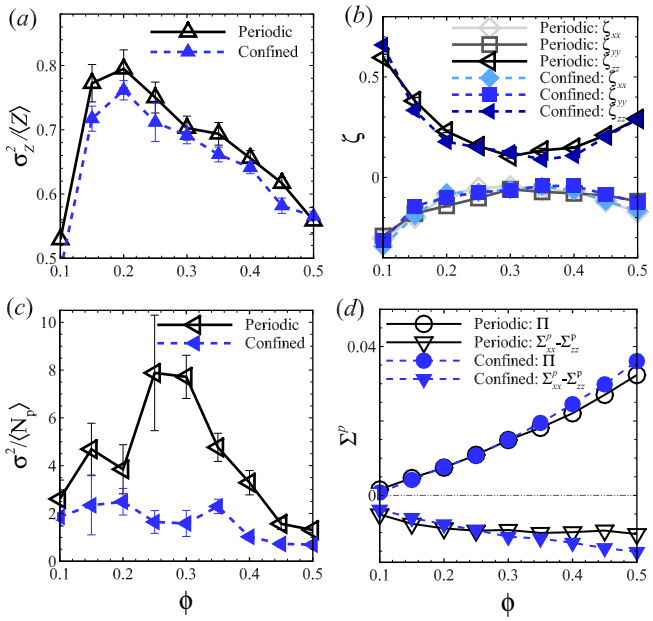

Fig. 10 (Colour online) Effects of confinement on multiscale responses. Microscale: (a) the time-averaged coordination number fluctuation and (b) the time-averaged diagonal components of the deviatoric tensor at steady state. Mesoscale: (c) the number density fluctuation at steady state averaged over five expected values of $\langle N_p \rangle = 20, 30, 40, 50, 60$. Macroscale: (d) the particle pressure Π and the normal stress difference $\Sigma^p_{xx} - \Sigma^p_{zz}$.

4 Conclusions

We studied the multiscale characteristics of the structural formation in a suspension of dielectric spheres in an electric field from dilute to concentrated regimes using large-scale particle simulations. For the current simulation model, we used the fast smooth particle mesh Ewald algorithm to account for dipolar interactions and hydrodynamic interactions (capturing both near-field and far-field electric and hydrodynamic interactions) for large systems over a long time [12, 39].

The kinetics of structural evolution is studied by the RMS particle velocities and mean cluster size. There is a distinctive difference in temporal behavior of structural kinetics between the regimes of volume fraction. Unlike the dilute regime ($\phi < 25\%$), beyond the semi-dilute regime ($\phi > 25\%$), the particles tend to undergo the formation of larger structures directly without the initial formation of particle chains, eventually forming a large cellular network pattern.

At the microscopic level, the degree of structural anisotropy is evaluated by the deviatoric tensor based on the fabric tensor. The temporal behavior of these parameters is shown to depend on volume fraction. Although the initial increasing trend of anisotropy before reaching the most anisotropic state occurs for all volume fractions, their long-time behavior after this most anisotropic state varies with volume fraction. For a volume fraction as small as $\phi = 10\%$, the long-time variation of this state is negligible due to very weak interactions between highly anisotropic chains that are largely separated. For $15\% \leqslant \phi \leqslant 30\%$, the rearrangement and coalescence arise within structures to recover microscopic isotropy. In concentrated regimes ($\phi \geqslant 40\%$), the long-term structural evolution tends to arrest without any further changes in the microstructural features. At steady-state, the degree of microscopic anisotropy decreases up to $\phi = 30\%$ and then slightly increases as a volume fraction is further increased. The degree of microscopic heterogeneity is also evaluated by the coordination number fluctuation. Interestingly, it also exhibits a non-monotonic ϕ-dependence but follows the opposite trend to microscopic anisotropy. The degree of heterogeneity sharply increases up to $\phi \approx 20\%$ followed by a gentle decrease.

For a mesoscale measure, the degree of structural heterogeneity was measured by the number density fluctuation, which also displays a non-monotonic variation with volume fraction. Sim-

ilar to the microscopic heterogeneity, the degree of mesoscopic heterogeneity increases up to $\phi = 20\%$ or $\phi = 30\%$ and then decreases as a larger cellular-like network pattern is formed.

For a macroscopic measure, the particle-induced stress field was computed. Most of the normal stresses are negative and become more negative as approaching a steady state. However, the field normal stress initially becomes less negative for $\phi < 30\%$ and even becomes positive for $\phi = 10\%$. For semi-dilute and concentrated suspensions ($\phi > 30\%$), it still exhibits a decreasing trend as approaching a steady state. At steady-state, the normal stresses become more anisotropic with volume fraction and reach the most anisotropic state at $\phi \approx 25\%$. However, it remains almost at that state for $\phi > 30\%$, while particle pressure keeps increasing.

The present multiscale observations suggest that there is a transition in the multiscale responses at $\phi \approx 30\%$. At this volume fraction, the steady-state suspension structure is shown to be the most isotropic at the microscale, while its stress field is the most anisotropic at the macroscale. In addition, the heterogeneity of suspension structures becomes maximum at this volume fraction at both microscale and mesoscale. Although there clearly seems a mutual physical consequence that influences each other among three length scales at $\phi = 30\%$, such investigation will be included in future work.

Lastly, we explore the effects of confinement on structural formation. It should be noted that we excluded the DEP interactions between the particles and the boundaries. The confinement seems to effectively screen the mesoscopic response, while there are slight changes at the microscale. This screening effect is clearly observed at the transitional volume fraction, $\phi \approx 30\%$, where the strong mesoscopic heterogeneity disappears. This mesoscopic response via confinement appears to strongly affect the macroscopic stress anisotropy that keeps increasing with volume fraction, unlike the periodic suspension where it increases only until $\phi \approx 25\%$. The confinement effect on the mesoscopic and macroscopic features could suggest that the suspension has a more direct link between the mesoscale and macroscale, but detailed investigations will be included in future work. Nonetheless, the current multiscale understanding of structural formation can lead to control strategies for practical applications of electric-driven suspensions, such as for ER fluids.

Conflicts of interest

There are no conflicts to declare.

Acknowledgments

The authors gratefully acknowledge the financial support from the Collaboration Initiative and Interdisciplinary Research Grants at the University of Nebraska and in part from the National Science Foundation through a grant CBET-1936065. This work was completed utilizing the Holland Computing Center of the University of Nebraska, which receives support from the Nebraska Research Initiative.

Notes and references

1 T. B. Jones and T. B. Jones, *Electromechanics of particles*, Cambridge University Press, 2005.
2 M. Parthasarathy and D. J. Klingenberg, *Mater. Sci. Eng. R Rep.*, 1996, **17**, 57–103.
3 Y. Z. Dong, Y. Seo and H. J. Choi, *Soft Matter*, 2019, **15**, 3473–3486.
4 D. Saintillan, *Phys. Fluids*, 2008, **20**, 067104.
5 H. A. Pohl, *Dielectrophoresis: the behavior of neutral matter in nonuniform electric fields*, 1978.
6 R. Tao and J. Sun, *Phys. Rev. Lett.*, 1991, **67**, 398.
7 T. C. Halsey and W. Toor, *Phys. Rev. Lett.*, 1990, **65**, 2820.
8 J. E. Martin, J. Odinek and T. C. Halsey, *Phys. Rev. Lett.*, 1992, **69**, 1524.
9 J. E. Martin, R. A. Anderson and C. P. Tigges, *J. Chem. Phys.*, 1998, **108**, 3765–3787.
10 D. Klingenberg, F. Van Swol and C. Zukoski, *J. Chem. Phys.*, 1989, **91**, 7888–7895.
11 A. K. Agarwal and A. Yethiraj, *Phys. Rev. Lett.*, 2009, **102**, 198301.
12 J. S. Park and D. Saintillan, *Phys. Rev. E*, 2011, **83**, 041409.
13 A. Kumar, B. Khusid, Z. Qiu and A. Acrivos, *Phys. Rev. Lett.*, 2005, **95**, 258301.
14 D. J. Klingenberg, C. F. Zukoski and J. C. Hill, *J. Appl. Phys.*, 1993, **73**, 4644–4648.
15 W. Wen, X. Huang and P. Sheng, *Soft Matter*, 2008, **4**, 200–210.
16 U. Dassanayake, S. Fraden and A. van Blaaderen, *J. Chem. Phys.*, 2000, **112**, 3851–3858.
17 J. Melrose and D. Heyes, *J. Chem. Phys.*, 1993, **98**, 5873–5886.
18 K. Hass, *Phys. Rev. E*, 1993, **47**, 3362.
19 P. Sheng and W. Wen, *Annu. Rev. Fluid Mech.*, 2012, **44**, 143–174.
20 T. Hao, *Adv. Mater.*, 2001, **13**, 1847–1857.
21 H. Yamaguchi, X.-R. Zhang, X.-D. Niu and K. Nishioka, *J. Intell. Mater. Syst. Struct.*, 2010, **21**, 423–435.
22 B. Qian, G. H. McKinley and A. Hosoi, *Soft Matter*, 2013, **9**, 2889–2898.
23 J. Li, X. Liang, F. Liou and J. Park, *Sci. Rep.*, 2018, **8**, 1–11.
24 R. Tao, *J. Phys. Condens. Matter*, 2001, **13**, R979–R999.
25 S. Hardt, J. Hartmann, S. Zhao and A. Bandopadhyay, *Phys. Rev. Lett.*, 2020, **124**, 064501.
26 R. T. Bonnecaze and J. Brady, *J. Rheol.*, 1992, **36**, 73–115.
27 R. T. Bonnecaze and J. Brady, *J. Chem. Phys.*, 1992, **96**, 2183–2202.
28 D. Klingenberg, F. van Swol and C. Zukoski, *J. Chem. Phys.*, 1991, **94**, 6170–6178.
29 L. Marshall, C. F. Zukoski and J. W. Goodwin, *J. Chem. Soc., Faraday Trans. 1*, 1989, **85**, 2785–2795.
30 J. E. Van Der Hoeven, E. B. Van Der Wee, D. M. De Winter, M. Hermes, Y. Liu, J. Fokkema, M. Bransen, M. A. Van Huis, H. C. Gerritsen, P. E. De Jongh *et al.*, *Nanoscale*, 2019, **11**, 5304–5316.

31 S. Jamali, G. H. McKinley and R. C. Armstrong, *Phys. Rev. Lett.*, 2017, **118**, 048003.

32 S. Jamali, R. C. Armstrong and G. H. McKinley, *Phys. Rev. Lett.*, 2019, **123**, 248003.

33 V. Michailidou, G. Petekidis, J. Swan and J. Brady, *Phys. Rev. Lett.*, 2009, **102**, 068302.

34 W. Fornari, L. Brandt, P. Chaudhuri, C. U. Lopez, D. Mitra and F. Picano, *Phys. Rev. Lett.*, 2016, **116**, 018301.

35 R. Jeanneret, D. O. Pushkin and M. Polin, *Phys. Rev. Lett.*, 2019, **123**, 248102.

36 C. Jin, Y. Chen, C. C. Maass and A. J. Mathijssen, *Phys. Rev. Lett.*, 2021, **127**, 088006.

37 A. P. Gast and C. F. Zukoski, *Adv. Colloid Interface Sci.*, 1989, **30**, 153–202.

38 J. S. Park and D. Saintillan, *J. Fluid Mech.*, 2010, **662**, 66–90.

39 S. Mirfendereski and J. S. Park, *J. Fluid Mech.*, 2019, **875**, year.

40 S. Kim and S. J. Karrila, *Microhydrodynamics: Principles and selected applications*, Courier Corporation, 2013.

41 W. Ristenpart, I. A. Aksay and D. Saville, *J. Fluid Mech.*, 2007, **575**, 83–109.

42 H. Hasimoto, *J. Fluid Mech.*, 1959, **5**, 317–328.

43 D. Saintillan, E. Darve and E. S. Shaqfeh, *Phys. Fluids*, 2005, **17**, 033301.

44 A. Sierou and J. F. Brady, *J. Fluid Mech.*, 2001, **448**, 115–146.

45 S. Mirfendereski and J. S. Park, *J. Rheol.*, 2021, **65**, 13–26.

46 H. See and M. Doi, *J. Phys. Soc. Japan*, 1991, **60**, 2778–2782.

47 E. M. Sevick, P. A. Monson and J. M. Ottino, *J. Chem. Phys.*, 1988, **88**, 1198–1206.

48 M. Satake, *Proc. US-Japan Seminar on Continuum Mech. Stat. Appr. Mech. Granul. Mater., Sendai*, 1978, 203–215.

49 M. M. Mehrabadi, S. Nemat-Nasser and M. Oda, *Int. J. Numer. Anal. Methods Geomech.*, 1982, **6**, 95–108.

50 T. Olsen and K. Kamrin, *Soft Matter*, 2015, **11**, 3875–3883.

51 T. Olsen, A. Helal, G. H. McKinley and K. Kamrin, *Soft Matter*, 2016, **12**, 7688–7697.

52 Y. Yurkovetsky and J. F. Morris, *J. Rheol.*, 2008, **52**, 141–164.

53 A. Deboeuf, G. Gauthier, J. Martin, Y. Yurkovetsky and J. F. Morris, *Phys. Rev. Lett.*, 2009, **102**, 108301.